A numerical study of compressible turbulent boundary layers

M. Lagha, J. Kim, J. D. Eldredge, and X. Zhong
Department of Mechanical and Aerospace Engineering, UCLA, 420 Westwood Plaza, Los Angeles, California 90095-1597, USA

(Received 13 August 2010; accepted 20 December 2010; published online 25 January 2011)

Compressible turbulent boundary layers with free-stream Mach number ranging from 2.5 up to 20 are analyzed by means of direct numerical simulation of the Navier–Stokes equations. The fluid is assumed to be an ideal gas with constant specific heats. The simulation generates its inflow condition using the rescaling-recycling method. The main objective is to study the effect of Mach number on turbulence statistics and near-wall turbulence structures. The present study shows that supersonic/hypersonic boundary layers at zero pressure gradient exhibit close similarities to incompressible boundary layers and that the main turbulence statistics can be correctly described as variable-density extensions of incompressible results. The study also shows that the spanwise streak's spacing of 100 wall units in the inner region ($y^+ \approx 15$) still holds for the considered high Mach numbers. The probability density function of the velocity dilatation shows significant variations as the Mach number is increased, but it can also be normalized by accounting for the variable-density effect. The compressible boundary layer also shows an additional similarity to the incompressible boundary layer in the sense that without the linear coupling term, near-wall turbulence cannot be sustained. © *2011 American Institute of Physics*. [doi:10.1063/1.3541841]

I. INTRODUCTION

The design of supersonic and hypersonic vehicles depends critically on the accurate prediction of turbulent flow characteristics in high Mach number boundary layers. Basic knowledge and understanding of both aerodynamic and thermodynamic phenomena are the prerequisites in order to use design tools effectively. The understanding of complex flow phenomena can best be obtained through a coordinated study involving both computational and theoretical analyses. Relatively few numerical simulations of a turbulent supersonic boundary layer are available in the literature. Most of these studies were primarily focused on the effects of compressibility on turbulence statistics at relatively low Mach numbers (≤ 5). Very few studies aimed at improving the understanding of the fundamental physics of supersonic boundary layers have been conducted.

It is known that for supersonic flows with moderate Mach numbers, the direct effects of compressibility on wall turbulence at zero pressure gradient are small, the most notable differences being due to the variation of the thermodynamic properties across the layer. This is known as the Morkovin hypothesis. All available experimental data (see Ref. 1 and references therein) confirm indeed that supersonic boundary layers at zero pressure gradient exhibit close similarities to incompressible ones and that the main turbulence statistics can be correctly predicted as variable-density extensions of incompressible results.

These similarities have been confirmed by recent direct numerical simulations, which include the extended temporal simulation of Maeder *et al.*[2] ($M_\infty = 2.5$), the quasiperiodic simulation of Guarini *et al.*[3] ($M_\infty = 2.5$), and the fully spatial simulations of Martin[4] (M_∞ up to 8) and Pirozzoli *et al.*[5] ($M_\infty = 2.25$). These studies have further confirmed the validity of the van Driest transformation for the mean velocity profile and that the distributions of the density-scaled root-mean-square fluctuations of the velocity and vorticity closely follow the universal distribution found in the incompressible case.

Regarding fundamental physics of turbulent flow, most of our present understanding has been achieved due to a great deal of work conducted over the past few decades on incompressible flows. The fundamental physics of high Mach number turbulent boundary layers is, however, not well understood. Knowledge obtained from experimental studies is limited to the large-scale motions in the outer layer, mainly due to difficulties in resolving the very small flow scales found at the high Reynolds numbers typical of supersonic experimental arrangements.

The objective of the present study is to investigate the effects of high Mach number on turbulent boundary layers. The present paper is organized as follows. In Sec. II, the numerical methods, including the generation of inflow boundary conditions, are presented. The effects of Mach number on various turbulence statistics and turbulence structures are presented in Sec. III, followed by a summary and concluding remarks in Sec. IV. In this paper, we use x, y, and z to denote the streamwise, wall-normal, and spanwise directions, respectively, and u, v, and w to denote the velocity components in x, y, and z directions.

II. NUMERICAL PROCEDURES

A. The governing equations

The compressible Navier–Stokes equations are solved in conservative form, nondimensionalized with the free-stream quantities (ρ_∞, T_∞, U_∞, and μ_∞) as given in Ref. 2. For all cases, $\rho_\infty = 0.003\,937$ kg m^{-3}, $T_\infty = 161.5$ K, and

TABLE I. Simulation parameters.

M_∞	2.5	5	7.5	10	15	20
$R_{\delta_{99}}$	24 500	98 000	294 000	632 058	1 969 104	5 119 672
$R_\tau \pm 10$	340	300	310	300	302	345
U_∞ (m/s)	636	1 272	1 908	2 544	3 817	5 089
u_τ / U_∞	0.052	0.0558	0.0607	0.0613	0.0634	0.0644

$\mu_\infty = 1.1011 \times 10^{-5}$ kg m^{-1} s^{-1}, while U_∞ is increased as shown in Table I. The lengths are nondimensionalized using the boundary layer thickness at the inlet δ_{99} and the time by δ_{99}/U_∞. The computational Reynolds number $R_{\delta_{99}} = \delta_{99}\rho_\infty U_\infty / \mu_\infty$ is given in Table I for each free-stream Mach number M_∞. The value of this Reynolds number was adjusted such that it gives approximately the same Reynolds number based on the friction velocity R_τ as the Mach number is varied. The ratio of specific heats γ is assumed to be constant and equal to 1.4. The perfect gas state equation reads under this normalization as $\gamma M_\infty^2 p = \rho T$, where p is the pressure, ρ is the density, and T is the temperature. The dynamic viscosity μ obeys Sutherland's law: $\mu(T) = T^{3/2}(1+S)/(T+S)$, with $S = 110.4K/T_\infty$. The Prandtl number is Pr=0.72.

The compressible Navier–Stokes equations are solved using a shock-capturing hybrid finite-difference scheme.[6] Conventional finite-difference schemes are not suitable for the numerical simulations of compressible flows since high gradient regions generate large spurious oscillations. The weighted essentially nonoscillatory (WENO) scheme has been proven to be efficient for some test problems.[7] However, due to the way the Euler flux are evaluated, this scheme is computationally expensive and highly dissipative. Therefore, problems involving a few number of shocks and a large number of complex structures in the smooth regions require less dissipative and computationally more efficient numerical schemes.

We use an alternative approach, where high gradient regions are resolved by a WENO scheme and the smooth region are computed using a less dissipative and more efficient finite-difference scheme. Around high gradient regions, the Eulerian fluxes are computed using a fifth-order WENO decomposition/reconstruction,[7] whereas in the smooth regions, they are discretized by means of a fifth-order upwind scheme with global Lax–Friedrichs flux splitting. The choice of using one scheme instead of the other for a given cell is based on the smoothness property of the solution. In the present work, we have used the smoothness indicator used in Ref. 8, which reads for a given cell and a given quantity f

$$r_{j+1/2} = \min(r_j, r_{j+1}),$$

where

$$r_j = \frac{2\Delta f_{j+1/2}\Delta f_{j-1/2} + \epsilon}{(\Delta f_{j+1/2})^2 + (\Delta f_{j-1/2})^2 + \epsilon}.$$

The ϵ is a positive real number and Δ denotes the standard difference operator. Above a certain threshold r_{thres}, the solution is considered as nonsmooth and the WENO scheme is applied. The task of chosen this threshold is simplified since, from the definition above, the value returned by the smoothness indicator is bounded and we have $r_{j+1/2} \in [0,1]$.

The viscous fluxes are approximated using a sixth-order finite-difference scheme and the time integration is performed by means of a classical four-stage fourth-order explicit Runge–Kutta scheme. This numerical scheme was validated against various compressible flows and the interested reader is referred to Lagha *et al.*[6] for further details.

The parameters of the simulations are given in Table I. First, our approach with $M_\infty = 2.5$ is validated against published results. Then, two cases with higher free-stream Mach numbers $M_\infty = 10$ and $M_\infty = 20$ are considered. It should be noted that the high Mach number flows considered in the present paper (e.g., $M_\infty = 20$ flow over a flat plate with the perfect gas law) are not realistic for various reasons. First, real gas effects must be accounted for at high Mach numbers. A study of real gas effects at high Mach number is currently underway. It is worth noting in passing, however, that real gas effects are not present in most ground-based hypersonic experimental facilities because of relatively low stagnation temperatures. Also, it should be pointed out that most boundary layers in a realistic situation will be behind a bow shock and therefore the free-stream Mach number may be well below $M_\infty = 20$. Nevertheless, the present problem, its somewhat academic nature notwithstanding, provides an excellent test case for studying the effect of high Mach number on turbulent boundary layer flows.

B. Inflow boundary conditions

The generation of a turbulent inflow for the numerical simulation of a boundary layer is in itself an issue, owing to the difficulty of obtaining a physical turbulent flow at a reasonable computational cost. Different approaches, including temporal boundary layer (TDNS), extended TDNS, and spatial boundary layer, have been developed. In the latter case, the simulation generates its own inflow conditions by rescaling the flow field at a downstream station x_{re} and prescribing it at the inlet. This method was applied by Lund *et al.*[9] for an incompressible boundary layer and its extension to the compressible flow was developed by Urbin and Knight.[10] Further development of the method has been carried out (among others, Refs. 11–14). The inlet profile is obtained through a blending between two profiles, one for the inner region and another for the outer region. If the initial condition is not an already turbulent state taken from another simulation, a mismatch between the inner and outer region can occur at the inlet and the flow downstream will not reach a physical state.

Moreover, empirical formulas are used to approximate the value (at the inlet) of x-dependent local quantities, such as the friction velocity and the boundary layer thickness. Additionally, the friction velocity at the inlet can drift away from the correct value, leading to a temporal drift of the simulation (see Ref. 12).

In this section, we present a systematic method to obtain a supersonic/hypersonic turbulent boundary layer starting from a laminar flow field. The main idea is to use only quantities that are slowly streamwise dependent, such as Coles' parameter. The mean velocity profile at the inlet across the whole boundary is obtained through a composite profile. Some parameters of this composite profile will be adjusted during the simulation according to the downstream evolution of the flow. First, the van Driest velocity u_{vd} is defined by a density-weighted transformation

$$u_{\mathrm{vd}} = \int_0^{\bar{u}} \left(\frac{\bar{\rho}}{\rho_{\mathrm{w}}}\right)^{1/2} d\bar{u}.$$

The mean quantities (averaged in the spanwise direction) are denoted by an overbar and the subscript "w" refers to wall quantities, which are also averaged in the spanwise direction. The subscript "re" denotes the recycled downstream station and "in" denotes the inlet.

The mean temperature profile of the initial condition is estimated using the Crocco–Busemann approximation across the entire boundary layer $\bar{T}_{\mathrm{in}}/T_\infty = T_{\mathrm{w}}/T_\infty - r(\gamma-1)/2M_\infty^2(\bar{u}_{\mathrm{in}}/U_\infty)^2$, with $r=0.82$.[14] Because the pressure is nearly constant (except in the region very near the wall) throughout the boundary layer, the mean density profile can be deduced with the perfect gas law: $\bar{\rho}_{\mathrm{in}}/\rho_\infty = T_\infty/\bar{T}_{\mathrm{in}}$.

The composite profile uses Reichardt's inner layer solution and Finley's wake function[3]

$$u_{\mathrm{vd}}^+ = \frac{1}{k}\log(1+ky^+) + \alpha\left(1 - e^{-y^+/a} - \frac{y^+}{a}e^{-by^+}\right) + \frac{1}{k}\left[\left(\frac{y^+}{\delta_{99}^+}\right)^2 - \left(\frac{y^+}{\delta_{99}^+}\right)^3 + 6\Pi\left(\frac{y^+}{\delta_{99}^+}\right)^2 - 4\Pi\left(\frac{y^+}{\delta_{99}^+}\right)^3\right],$$

with

$$y^+ = yu_\tau/\nu_{\mathrm{w}}, \quad \delta_{99}^+ = R_\tau = \delta_{99}u_\tau/\nu_{\mathrm{w}}, \quad a = 11,$$

$$b = 0.33, \quad \alpha = (-1/k)\log(k) + C.$$

The values of the constants k and C are similar to the incompressible values, i.e., $C=4.7$ and $k=0.4$.

To construct the profile, we need δ_{99}, T_{w}, and an estimation for the friction velocity u_τ. The boundary layer thickness δ_{99} is obtained by fixing $R_{\delta_{99}} = \delta_{99}\rho_\infty U_\infty/\mu_\infty$ at the inlet. Then, the temperature at the wall is estimated as $T_{\mathrm{w}} = 1 + 0.896(\gamma-1)/2M_\infty^2$, which gives an estimation of ν_{w}. Coles' parameter is chosen as $\Pi=0.1$ (usually $\Pi \in [0.1, 0.5]$) and we solve for the friction velocity u_τ, knowing that at $y^+ = \delta_{99}^+$, the composite profile is equal to the free-stream velocity

$$\frac{1}{k}\log(1+k\delta_{99}^+) + \alpha\left(1 - e^{-\delta_{99}^+/a} - \frac{\delta_{99}^+}{a}e^{-b\delta_{99}^+}\right) + \frac{2\Pi}{k} = u_{\mathrm{vd}}^{\infty,+}.$$

Then, during the simulation, we estimate the new value of Π by solving the above equation at a downstream location x_{re} (where the friction velocity is now computed from the simulation and with the local value of δ_{99}). The friction velocity is re-estimated at the inlet by solving the above equation with the new value of Π. The new composite profile is then reconstructed at the inlet. The procedure is performed only two times, the first time with the chosen $\Pi=0.1$ and the second time with the estimated Π. Further refinement is not necessary. Note that Pirozzoli *et al.*[15] estimated the wake law constant to be $\Pi=0.175$, whereas Guarini *et al.*[3] found $\Pi \approx 0.25$. In our case, we found a similar value of $\Pi \approx 0.2$ for $M_\infty = 2.5$.

The perturbations, denoted with a prime and computed by subtracting the mean value from the flow field, can be assumed to satisfy a similarity law across the boundary layer. Therefore, they are rescaled and introduced at the inlet according to, for example,

$$u'_{\mathrm{in}}(y) = u'_{\mathrm{re}}\left(\frac{\delta_{99}^{\mathrm{re}}}{\delta_{99}}y\right),$$

where $\delta_{99}^{\mathrm{re}}$ represents the boundary layer thickness at the rescaling station. The same procedure is applied to the spanwise w' and wall-normal v' perturbations and to the thermodynamic perturbations T' and ρ' (further details are given in Refs. 10 and 11). For all cases, the streamwise L_x, wall-normal L_y, and spanwise L_z extents of the domain are $L_x \times L_y \times L_z = 14\delta_{99} \times 5\delta_{99} \times 2\delta_{99}$. The recycling station is located at $x_{\mathrm{re}} = x_{\mathrm{in}} + 8\delta_{99}$. Two sponge regions are added near the outlet (starting at $x = x_{\mathrm{in}} + 13\delta_{99}$) and the top of the domain (starting at $y = 4\delta_{99}$) to prevent artificial reflections from the boundaries.[6,14] Periodic boundary condition is used in the spanwise direction. In all cases, the number of points in the streamwise, wall-normal, and spanwise directions is $N_x \times N_y \times N_z = 512 \times 128 \times 256$. The grid resolutions in wall units are $\Delta_x^+ \times \Delta_y^+ \times \Delta_z^+ \approx 8 \times 0.3 \times 3$. A hyperbolic stretching is used in the y-direction and at the boundary layer edge $\Delta_y^+ \approx 11$. Higher resolutions (up to $1024 \times 180 \times 512$) were used to validate the accuracy of the simulations.

III. RESULTS

A. Mean flow and turbulence fluctuations

To validate the present simulation, the computed mean velocity, Reynolds stress, and the root-mean-square (rms) of the velocity and vorticity components are compared with the results of Guarini *et al.*[3] at $M_\infty = 2.5$. A few other studies of boundary layers at this Mach number or similar Mach numbers have been made recently, each conducted with different approaches (temporal and spatial simulations).[2,4,5,16] All the following results are computed at the recycling station $x_{\mathrm{re}} = x_{\mathrm{in}} + 8\delta_{99}$.

The distribution of the van Driest-transformed mean streamwise velocity, expected to satisfy the incompressible logarithmic law, is shown in a semilogarithmic plot in Fig. 1. The linear scaling in the viscous sublayer ($u_{\mathrm{vd}}^+ = y^+$) and the

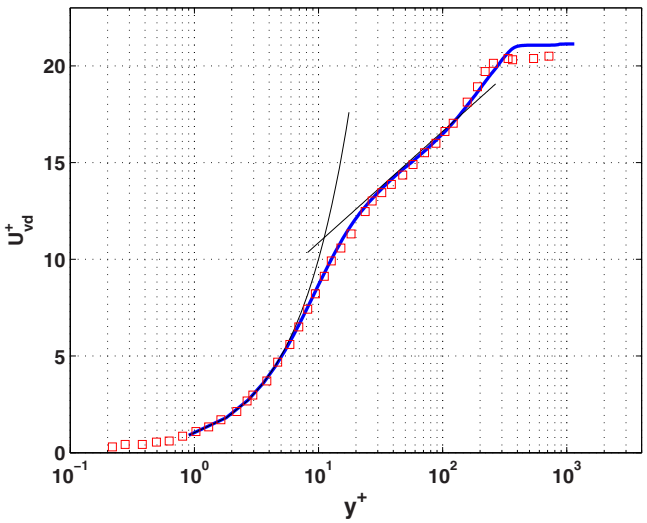

FIG. 1. (Color online) Mean velocity profile for $M_\infty=2.5$. Symbols correspond to Ref. 3 results.

logarithmic scaling in the overlap region $[u^+_{vd}=(1/k)\log y^+ +5.1, k\approx 0.4]$ are also plotted as references. The figure shows that the viscous sublayer law holds up to $y^+\approx 5$ and the logarithmic region extends from $y^+\approx 40$ to $y^+\approx 140$.

The distributions of the density-scaled Reynolds-stress components $(\sqrt{\bar{\rho}/\rho_w}\sqrt{u_i'^2}/u_\tau)$ are shown in Fig. 2 and they agree well with the DNS (Direct Numerical Simulations) data of Ref. 3. Here u_i' denotes u', v', and w' for $i=1,2,3$. A similar agreement holds for the Reynolds stress $\frac{\bar{\rho}}{\rho_w}\overline{u'v'}/u_\tau^2$. Note that this density scaling is equivalent to the local scaling since $\sqrt{\bar{\rho}/\rho_w}\sqrt{u_i'^2}/u_\tau = \sqrt{u_i'^2}/u_\tau^*$, where the y-dependent friction velocity $u_\tau^*(y) \equiv u_\tau\sqrt{\rho_w/\bar{\rho}(y)}$ takes into account the mean property variations (e.g., Refs. 17 and 18).

Figure 3 shows the distribution of the computed rms of the vorticity components normalized by the friction velocity and the kinematic viscosity at the wall $(\omega_i^+=\sqrt{\overline{\omega_i'^2}}\nu_w/u_\tau^2)$ as used in Ref. 3. Here, ω_i' denotes ω_x', ω_y', and ω_z' for $i=1,2,3$, respectively. This scaling collapses the rms of the

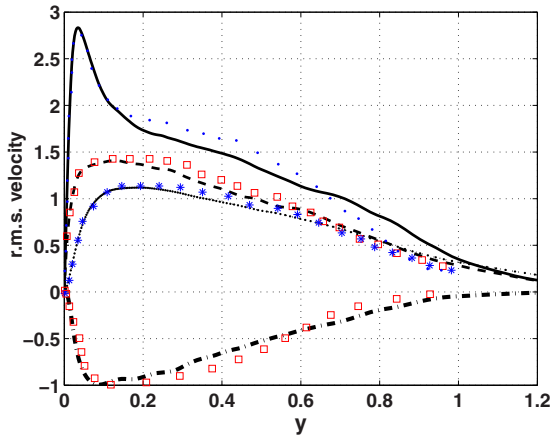

FIG. 2. (Color online) rms of the scaled streamwise (—), spanwise (- - -), and wall-normal (.....) velocity fluctuations. Reynolds shear stress (-.-.-.). Symbols correspond to Ref. 3 results. $M_\infty=2.5$.

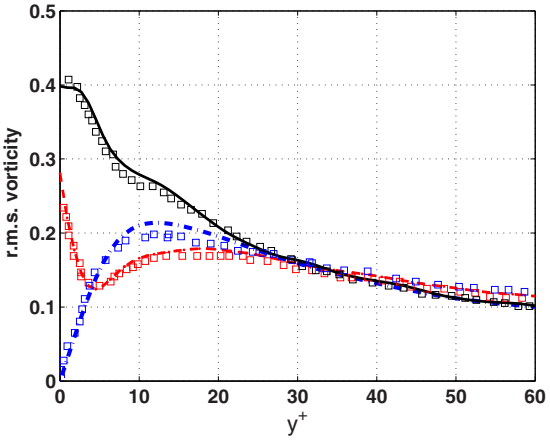

FIG. 3. (Color online) rms of the scaled vorticity fluctuation components: ω_x' (- - - -), ω_y' (-.-.-.-), and ω_z' (—). Symbols correspond to Ref. 3 results. $M_\infty=2.5$.

vorticity fluctuation components for different Mach numbers. However, other scaling possibilities exist. A possible scale is to use the local friction velocity u_τ^* and the mean viscosity $\sqrt{\overline{\omega_i'^2}}\bar{\nu}(y)/(u_\tau^*)^2$, which is equivalent to $\omega_i^+(\bar{\rho}/\rho_w)\times(\bar{\nu}/\nu_w)=\omega_i^+\bar{\mu}/\mu_w$. Using Sutherland's law and assuming that $\bar{T}+S\approx\bar{T}$ (especially near the wall) gives $\bar{\mu}/\mu_w \approx(\rho_w/\bar{\rho})^{1/2}$ and, therefore, the scaling $\omega_i^+(\rho_w/\bar{\rho})^{1/2}$. Another possibility is to use the local friction velocity u_τ^* but use the kinematic viscosity at the wall, as in $\sqrt{\overline{\omega_i'^2}}\nu_w/(u_\tau^*)^2$, which is equivalent to the scaling $\omega_i^+\bar{\rho}/\rho_w$. However, we have found that the scaling used by Ref. 3 gives a better collapse (see Fig. 8 below). This might be due to the fact that in this scaling, the density at the wall is replaced by the mean density, whereas the dynamic viscosity is taken at the wall, which is equivalent to $\sqrt{\overline{\omega_i'^2}}(\mu_w/\bar{\rho})/(u_\tau^*)^2 = \sqrt{\overline{\omega_i'^2}}(\mu_w/(\rho_w u_\tau^2))(\rho_w/\bar{\rho})(\sqrt{\bar{\rho}/\rho_w})^2=\sqrt{\overline{\omega_i'^2}}\nu_w/u_\tau^2=\omega_i^+$.[19]

For $y^+\geq 30$, the vorticity fluctuations become nearly isotropic $(\omega_x'\approx\omega_y'\approx\omega_z')$. Consistent with the DNS data in the literature, ω_x' attains a peak at $y^+\approx 16$ and ω_y' has its maximum at $y^+\approx 12$. The computed results show also that ω_x' has a local minimum at about $y^+=5$ before it attains its maximum value at the wall. This behavior is usually attributed to

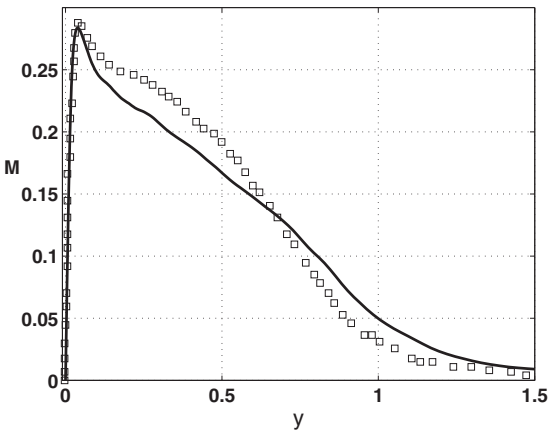

FIG. 4. The turbulent Mach number. Symbols correspond to Ref. 3 results. $M_\infty=2.5$.

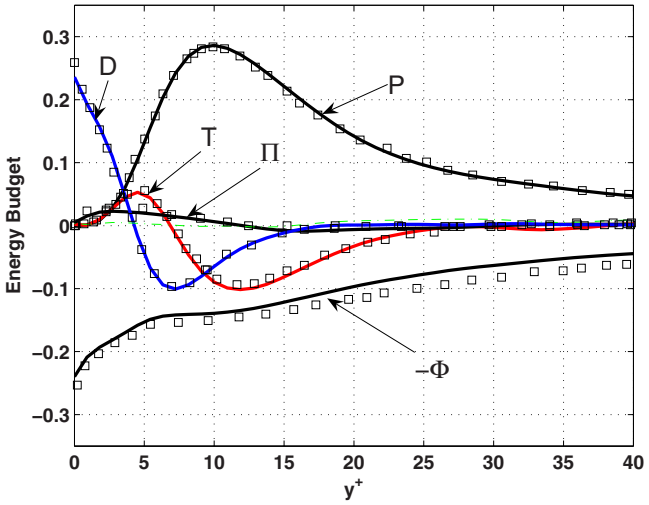

FIG. 5. (Color online) Turbulent kinetic energy budget. Letters are P, production term; T, turbulent transport; Π pressure term; D, viscous diffusion; and $-\Phi$, viscous dissipation. Lines correspond to simulation results. Symbols correspond to Ref. 3 results. The green dashed-dotted line corresponds to the sum of the five terms.

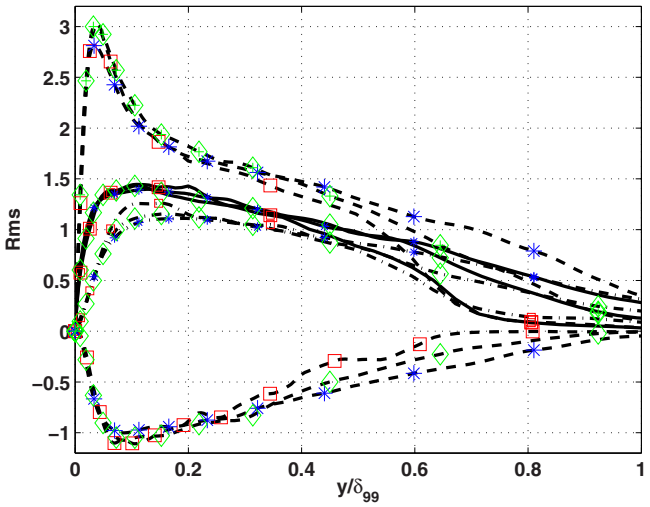

FIG. 7. (Color online) rms of the streamwise (- - - -), spanwise (—), and wall-normal (-.-.-.-) velocity fluctuations, together with the Reynolds stress (- - - -). M_∞=2.5 (*), 10 (◇), and 20 (□).

the presence of streamwise vortices in the wall region. The location of the local maximum corresponds to the average location of the center of the streamwise vortices. Kim *et al.*[20] have estimated that the centers of the streamwise vortices are located on the average at $y^+ \approx 20$ and they have a radius $r^+ \approx 15$. This observation is further developed in a companion paper.

The turbulent Mach number, defined as $M_t = \sqrt{\overline{u_i' u_i'}}/\bar{c}$, where $\bar{c}$ is the local speed of sound, is given in Fig. 4. The peak value of M_t is approximately 0.3, in agreement with Ref. 3. The effect of the Mach number on this quantity is addressed in the next section.

To further assess the quality of the simulations, the budget of the turbulent kinetic energy was compared to the literature results. This energy is defined as $k = 1/2\overline{\rho u_i'' u_i''}/\bar{\rho}$, where the superscript refers to fluctuations from the Favre averages, commonly used to simplify the resulting energy equation. The explicit forms of the different terms are given in Ref. 3. Namely, P is the rate of generation of turbulent kinetic energy by velocity gradients, T is the turbulent transport, Π is the pressure diffusion and dilatation, D is the viscous diffusion, and $-\Phi$ is the viscous dissipation. Figure 5 compares the distributions of these different terms, after normalization by the wall quantity $\rho_w u_\tau^4 R_{\delta_{99}}/\nu_w$,[2] to the DNS data of Guarini *et al.* and confirms the quality of the present simulation. Note that the contribution from the convective terms was not computed directly, but it is considered to be negligibly small since the balance of the terms shown in Fig. 5 is nearly zero (dashed line in Fig. 5).

Finally, the results for the higher Mach numbers M_∞ =10 and M_∞=20 are given in Figs. 6–9. To increase the Mach number, the free-stream temperature is maintained fixed but the velocity U_∞ is increased, as shown in Table I. Then, the free-stream Reynolds number $R_{\delta_{99}}$ is adjusted (by changing δ_{99}), so that $R_\tau = \delta_{99} u_\tau/\nu_w$ keeps the same value. The targeted value was R_τ=350, which is high enough to give a developed logarithmic region to the mean profile.

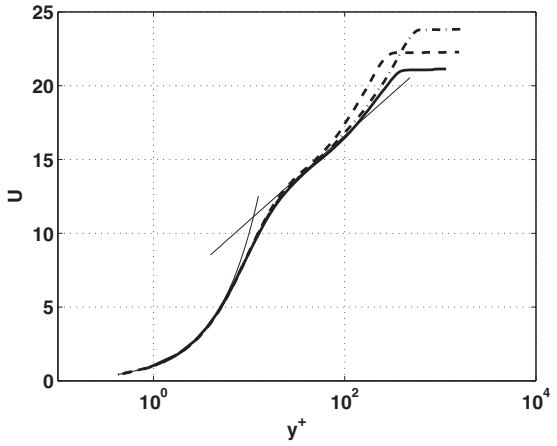

FIG. 6. Mean velocity profiles for M_∞=2.5 (—), 10 (-.-.-.-.-), and 20 (- - - -).

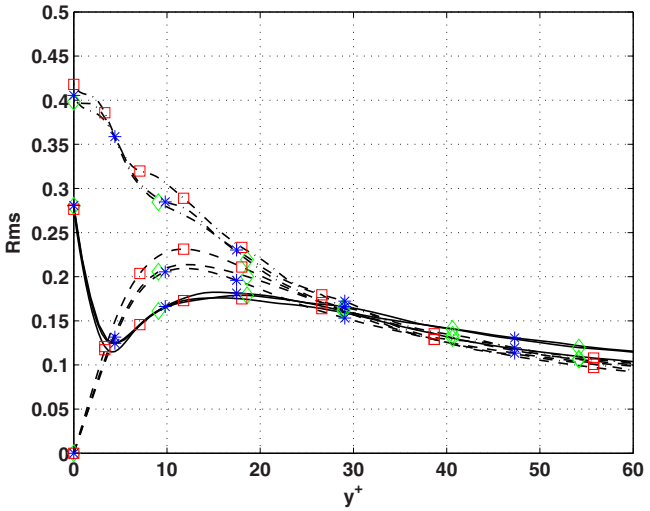

FIG. 8. (Color online) rms of the vorticity component fluctuations ω_x' (—), ω_z' (-.-.-.), and ω_y' (- - - -). M_∞=2.5 (*), 10 (◇), and 20 (□).

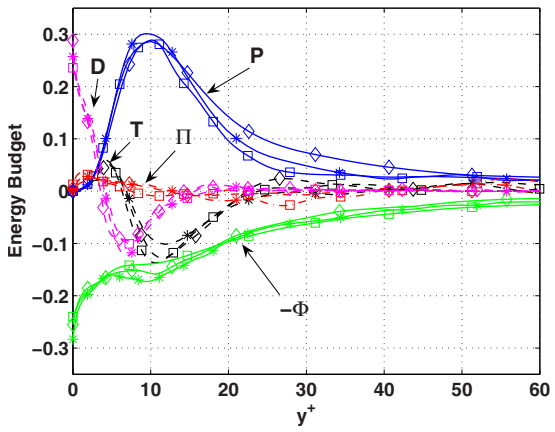

FIG. 9. (Color online) Energy budget. $M_\infty=2.5$ (□), 10 (◇), and 20 (*).

Note that since R_τ is similar for these cases, the domain extent in wall units is similar: $L_x^+\times L_y^+\times L_z^+\approx 4100\times 500\times 760$.

The results shown in Figs. 6–9 illustrate that turbulent boundary layers at $M_\infty=10$ and $M_\infty=20$ exhibit close similarities with the low supersonic case $M_\infty=2.5$ and that the main turbulence statistics can be correctly described as variable-density extensions of incompressible results.

B. Turbulent Mach number and fluctuating Mach number

In addition to the turbulent Mach number (M_t), we also examined the rms perturbations of the local Mach number, called the fluctuating Mach number M', since it presents different information in compressible flows.

The turbulent Mach number is shown in Fig. 10 (left) for different M_∞. Its maximum value slowly increases with M_∞, in agreement with the observation of Martin.[4] Its value is about 0.6 for $M_\infty=20$ and is located near the wall. The fluctuating Mach number M' is, however, more sensitive to M_∞. For low M_∞ (≤ 5), the maximums of both M_t and M' are approximately similar, but for higher M_∞, they become different. Additionally, M' starts to build a second maximum which moves away from the wall, as seen in Fig. 10 (right), in agreement with the observations of Spina *et al.*[21]

To study the origin of this behavior and, more specifically, to differentiate between a true compressibility effect and a variable-property effect, we follow the approach of Coleman *et al.*[17] They introduced a separate Mach number M_d in the temperature equation, referring to it as the dissipation Mach number. The temperature equation becomes

$$\frac{\partial T}{\partial t}+u_j\frac{\partial T}{\partial x_j}=-(\gamma-1)T\frac{\partial u_j}{\partial x_j}+\gamma\frac{\gamma-1}{R_{\delta_{99}}}M_\infty^2\tau_{ij}\frac{\partial u_i}{\partial x_j}$$

$$-\frac{\gamma}{R_{\delta_{99}}\,\mathrm{Pr}\,\rho}\frac{\partial \tilde{q}_j}{\partial x_j}+\mathcal{L},$$

where the heat-flux vector is $\tilde{q}_i=-\mu\partial T/\partial x_i$ and $\mathcal{L}=(M_d^2-M_\infty^2)\gamma(\gamma-1)\tau_{ij}/\rho R_{\delta_{99}}\partial u_i/\partial x_j$.

Setting $M_d\neq M_\infty$ is equivalent to adding a nonzero heat source/sink term $\mathcal{L}$ to the temperature equation. Such nonphysical simulations are used to determine the relative importance of turbulent-fluctuation and variable-property influences at a given M_∞, since cases with different mean temperature profiles (i.e., different mean property variations) at the same free-stream Mach number M_∞ can be considered.

In our current simulation, the governing equation for the total energy E becomes

$$\frac{\partial E}{\partial t}+\frac{\partial[u_i(E+p)+q_i]}{\partial x_i}=\left[\frac{\partial u_i\tau_{ij}}{\partial x_j}+\left(\frac{M_d^2}{M_\infty^2}-1\right)\tau_{ij}\frac{\partial u_i}{\partial x_j}\right],$$

where τ_{ij} is the stress tensor and is given by $\tau_{ij}=\mu/R_{\delta_{99}}(\partial u_i/\partial x_j+\partial u_j/\partial x_i-2/3\,\partial u_k/\partial x_k\delta_{ij})$. The heat flux is $q_i=-\mu/((\gamma-1)M_\infty^2\,\mathrm{Pr}\,R_{\delta_{99}})\partial T/\partial x_i$. Therefore, in a normal simulation, $M_\infty=M_d$, whereas in a nonphysical one, $M_\infty\neq M_d$.

For $M_\infty=M_d=2.5$, we have found that M' and M_t have similar values. However, by increasing the mean variation of the mean temperature by setting $M_d=7.5$, M' increases to roughly twice its initial value. Therefore, the apparent increase in the value of M' with M_∞ is not a true compressibility effect but, rather, is due to the variation of the mean

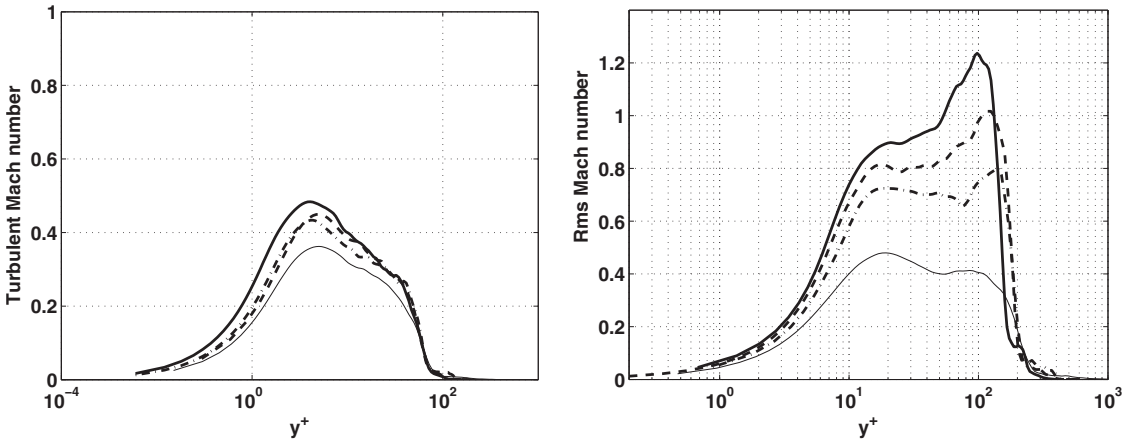

FIG. 10. Profiles of the turbulent Mach number M_t (left) and the fluctuating Mach number M' (right) for $M_\infty=5$ (thin solid line), $M_\infty=10$ (-.-.-.-), $M_\infty=15$ (- - - -), and $M_\infty=20$ (—). Without any scaling.

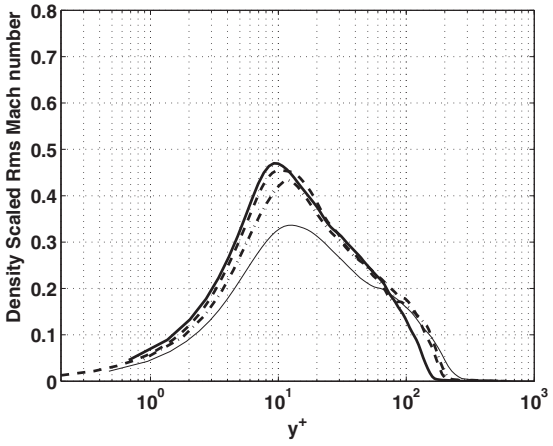

FIG. 11. Profiles of the fluctuating Mach number M'. Legends are similar to Fig. 10. Using the mean density scaling $M'\bar{\rho}/\rho_w$.

property. This suggests that the variation of M' is due to the variable-density effect. In fact, we have found that the simple scaling $M' \rightarrow M'\bar{\rho}/\rho_w$ collapses the profiles of M' for different M_∞ into a single one, as shown in Fig. 11. This scaling seems to work better for the hypersonic Mach numbers 10, 15, and 20.

C. Dilatation

The dilatation term $\vartheta \equiv \partial_x u + \partial_y v + \partial_z w$, which is zero for $M_\infty = 0$, is another measure of the effect of the Mach number (e.g., Refs. 22 and 23). The plot of the probability density function (pdf) of ϑ in Figs. 12 and 13 confirms the increase of the probability of observing higher values of $|\vartheta|$ with increasing free-stream Mach number. To check whether this behavior is a true compressibility effect or a variable-property effect, we have computed the pdf of ϑ for the nonphysical case $M_\infty = 2.5$ and $M_d = 7.5$. The result, shown in Fig. 12, suggests that the increase in the pdf tail is a variable-property effect since the pdf of this nonphysical case is very close to that of the physical case $M_\infty = 7.5$. This implies that a scaling using the mean density would collapse the different

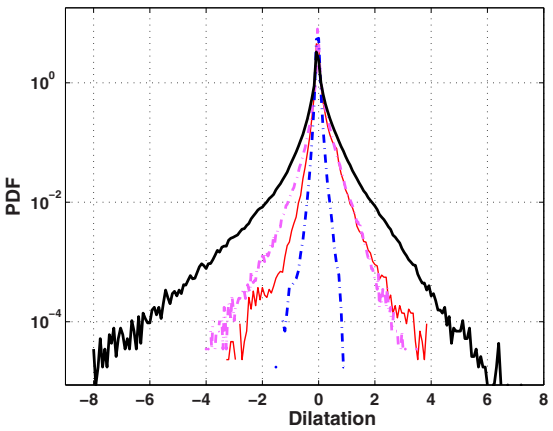

FIG. 12. (Color online) The pdf of the dilatation ϑ for $M_\infty = 2.5$ (-.-.-.-, blue line), $M_\infty = 7.5$ (- - - -, magenta line), and $M_\infty = 20$ (solid black line) in (x,y)-planes for different spanwise locations. The thin red line corresponds to the nonphysical simulation with $M_d = 7.5$ and $M_\infty = 2.5$. Without any scaling.

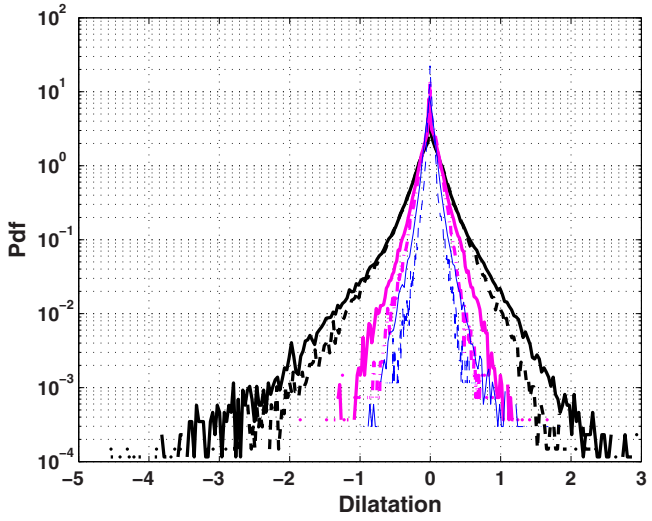

FIG. 13. (Color online) Legend similar to Fig. 12. The pdf is computed in (x,z)-planes corresponding to different wall-normal locations $y \in [0.1, 0.4]$. Without any scaling.

pdf curves. We have found in fact that by computing the pdf of $\vartheta\bar{\rho}$, the different pdf curves collapse (Figs. 14 and 15). It is worth noting that the collapse to a single curve of the compression part $(\vartheta \leq 0)$ of the different pdf curves is slightly better than the collapse of the dilatation part $(\vartheta \geq 0)$.

D. Turbulence structure

In a numerical study of channel flow, Coleman *et al.*[17] observed an increase with the Mach number of the streamwise coherence of the near-wall streaks (longer streaks). They showed that this modification of turbulence structure represents a confirmation of, and not an exception to, the Morkovin hypothesis, which postulates that at supersonic Mach numbers, only mean property variations are important and not the thermodynamic fluctuations. In fact, Coleman *et al.*[17] were able to show, using an artificial simulation with

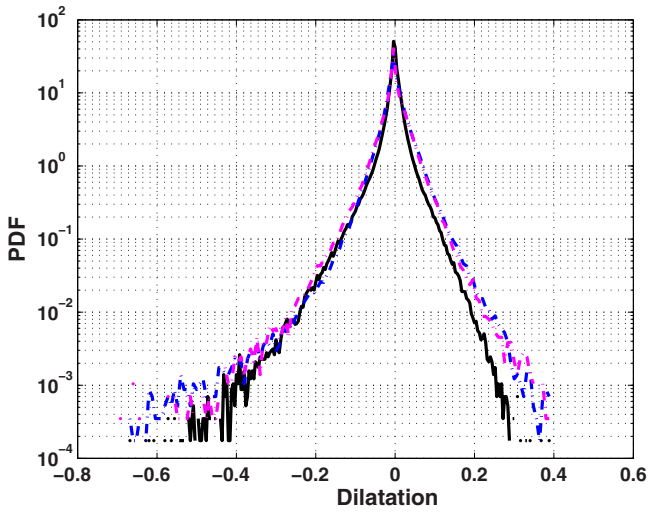

FIG. 14. (Color online) Legend similar to Fig. 12. Using the mean density scaling.

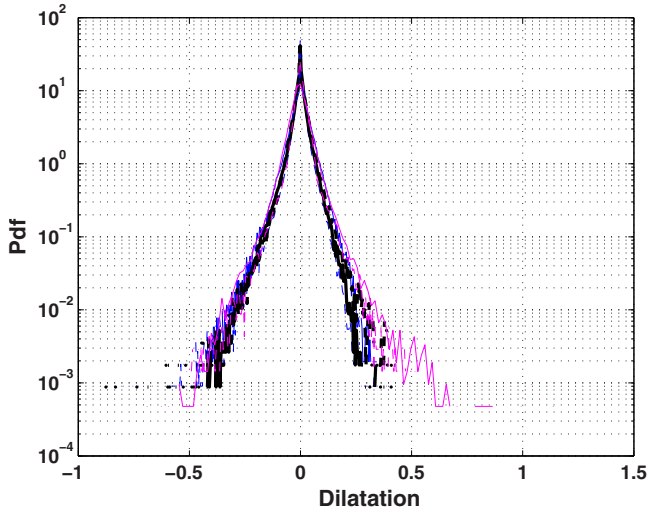

FIG. 15. (Color online) Legend similar to Fig. 13. Using the mean density scaling.

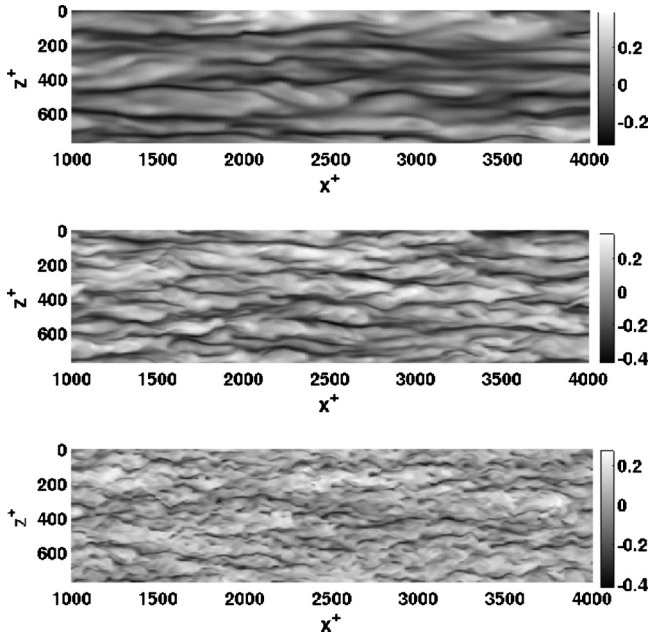

FIG. 16. Streamwise velocity perturbations for the three different wall temperatures at $y^+=15$. Top to bottom: $T_w/T_\infty=1$, $T_w/T_\infty=2.14$, and $T_w/T_\infty=11.6$.

constant density and temperature profiles, that the enhanced streak coherence has its source in the mean property variations. The method that they used, which was described earlier in this paper, consisted of differentiating between compressibility effects due to thermodynamic fluctuations and those caused by mean property variations using an artificial heat source defined by a dissipation Mach number. They concluded that nonzero near-wall gradients of mean properties are required for the streaks modification to occur. In other words, the enhanced streak coherence has its source in the mean property variations rather than in the thermodynamic fluctuations. A few conclusions can be drawn from this. First, the near-wall streaks become longer when the wall becomes colder, independently from the free-stream Mach number. This point was confirmed by Duan *et al.*[24] who performed a parametric study of a turbulent boundary layer by varying the temperature at the wall from $T_w/T_\infty=1$ (cold wall) to $T_w/T_\infty=5$ ($\approx T_{\text{adiab}}/T_\infty$). The free-stream Mach number was fixed at $M_\infty=5$. Second, the streaks become shorter when the wall is heated. Third, the streaks are not modified when the gradients of mean properties are zero, namely, for an adiabatic wall. To confirm the first two points, we have performed three isothermal simulations where the wall temperature T_w/T_∞ was varied but the free-stream Mach number was fixed to $M_\infty=2.5$. The considered wall temperatures are $T_w/T_\infty=1$ (cold wall), $T_w/T_\infty=2.14$ (near adiabatic value), and $T_w/T_\infty=11.6$ (hot wall). For the three cases, $R_\tau\approx 380$. The streamwise velocity perturbations in a horizontal plane located at $y^+=15$ are shown in Fig. 16 and they confirm the results of Refs. 17 and 24: the streaks become longer when the wall is cooled. They also become shorter when the wall is heated. Note that these results are presented in terms of viscous units since they are more suitable to describe near-wall structures.

It is worth noting that two inner layer parameters can be used to quantify these three isothermal simulations. The first parameter is the friction Mach number $M_\tau=u_\tau/c_w$, where c_w is the speed of sound based on the wall temperature. The second parameter is the nondimensional heat flux $\beta_q=-1/(\text{Pr}R_{\delta_{99}}\rho_w u_\tau)(d\bar{T}/dy)_w$.[17,25] The values of these parameters are given in Table II for the three different simulations. The value of β_q is negative when the heat transfer is from the flow to the wall (for the case with $T_w/T_\infty=1$). It is positive when the wall is heating the flow and, respectively, indicates moderate and strong heating conditions for the cases with $T_w/T_\infty=2.14$ and $T_w/T_\infty=11.6$.

To study the third point, that streaks are unaffected in the adiabatic case, we examined two-point correlations of the adiabatic simulations with three Mach numbers $M_\infty=2.5$, $M_\infty=7.5$, and $M_\infty=20$. To further study the role of R_τ, we have also performed two additional simulations for the $M_\infty=2.5$ case with $R_\tau\approx 200$ and $R_\tau\approx 1200$. For the latter case, the resolution used is $N_x\times N_y\times N_z=1024\times 180\times 256$. Although this resolution is marginal to capture all relevant scales in this high Reynolds number flow, it should be adequate for the present purpose of examining the dependence of the streak spacing on the Reynolds number and as such, this simulation was not used for any other purposes. In all cases, two-point correlations of the velocity perturbation u' in the streamwise direction are computed for a fixed wall-normal location $y^+=15$.

Figure 17 (left) shows that the two-point correlations for different Mach numbers collapse, indicating that the streak coherence remains the same. The streamwise length of the streaks, measured in terms of viscous units, is therefore independent of the Mach number. However, if it is measured in

TABLE II. Isothermal parameters.

T_w/T_∞	1	2.14	11.6
M_τ	0.0912	0.0896	0.055
β_q	−0.0498	+0.0012	+0.1422

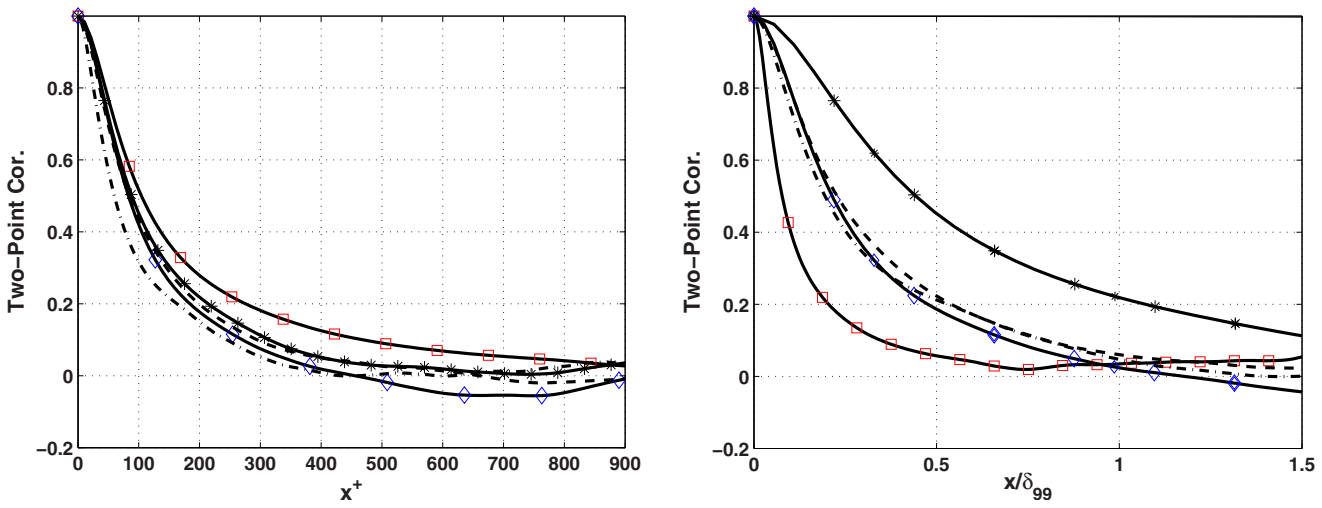

FIG. 17. (Color online) Two-point correlation of u' in the streamwise direction vs viscous unit x^+ (left) and vs x/δ_{99} (right). $M_\infty=20$ (-.-.-), $M_\infty=7.5$ (- - -), and $M_\infty=2.5$ (—). For $M_\infty=2.5$, $R_\tau\approx350$ ($\diamond$), $R_\tau\approx200$ (*), and $R_\tau\approx1200$ (■).

terms of the outer length scale δ_{99}, it becomes a function of the friction Reynolds number R_τ. The streak length in terms of x/δ_{99} decreases when R_τ increases, as shown in Fig. 17 (right). Therefore, one should use the viscous units to rule out the Reynolds number effect.

Finally, regarding the streaks width for an adiabatic wall, we examined two-point correlations in the spanwise direction of the streamwise velocity perturbation. At $y^+=15$, the typical spanwise streak spacing of 100 wall units is still valid, even at a free-stream Mach number of 20, as shown in Fig. 18. The minimum of the wall-normal velocity is found to be at 25 wall units and it represents the typical width of the streamwise vortices (e.g., Ref. 20).

Therefore, when computed at the same wall-normal location, say $y^+=15$, the streamwise and spanwise extents of the streaks, expressed in wall units, are not affected by the change in the free-stream Mach number for an adiabatic wall. This can also be deduced by comparing instantaneous snapshots of the streamwise velocity perturbations at $y^+=15$ for two different Mach numbers, as shown in Fig. 19. This concludes the proof of the third point.

To summarize, compared to an adiabatic simulation ($\beta_q=0$), the near-wall streaks are longer in a simulation with negative β_q and shorter in a simulation with positive β_q. We postulate that this parameter β_q (and eventually M_τ) can uniquely characterize isothermal simulations in the sense that two simulations with different free-stream Mach numbers but with the same β_q will have near-wall streaks with similar lengths.

E. Self-sustaining mechanism of near-wall turbulence

Kim and Lim[26] investigated the role of a linear coupling term (see definition below), which is a source of the non-normality of the eigenmodes of the linearized Navier–Stokes equations. They have found that near-wall turbulence in an incompressible channel flow decays without this linear coupling term. This shows that the maintenance of the turbulent state relies on a linear process. Whether the same behavior occurs in high Mach number compressible boundary layers is the subject of this section. For the wall-normal velocity v and the wall-normal vorticity ω_y, the linearized Navier–Stokes equations in the incompressible case can be written in an operator form

$$\begin{cases} \mathcal{L}_{OS}(v)=0 \\ \mathcal{L}_{Sq}(\omega_y)=\dfrac{dU_b}{dy}\partial_z v \end{cases},$$

where $\mathcal{L}_{OS}$ and $\mathcal{L}_{Sq}$ represent the Orr–Sommerfeld and Squire operators. The coupling term is given by $dU_b/dy\partial_z v$, where U_b is the mean velocity about which the Navier–Stokes equations are linearized. The nonlinear equations can be written in a similar form (see Ref. 26 for details). By running a fully nonlinear simulation and dropping only the linear coupling term, Kim and Lim[26] showed that the turbulence could not be sustained and the flow became laminar.

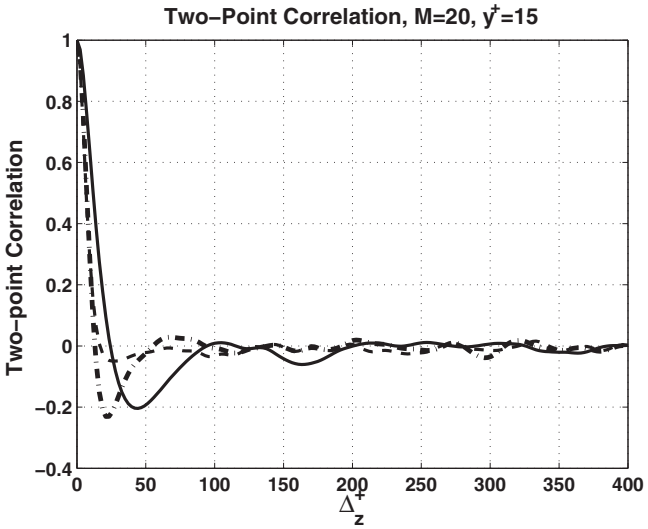

FIG. 18. Two-point correlations in the spanwise direction at $y^+=15$ for streamwise velocity perturbation (—), wall-normal velocity perturbation (-.-.-.), and streamwise vorticity (- - -). $M_\infty=20$.

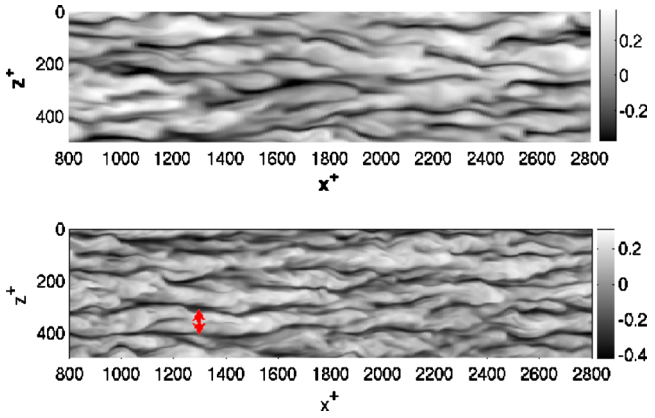

FIG. 19. (Color online) Streamwise velocity perturbation at $y^+=15$ for $M_\infty=2.5$ (top) and $M_\infty=20$ (bottom). The arrow indicates the typical streaks spacing of 100 wall units.

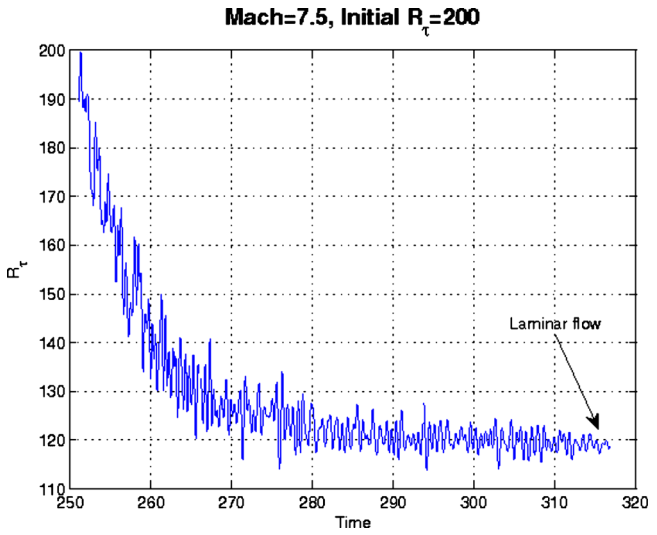

FIG. 20. (Color online) Simulation without the coupling term. $M_\infty=7.5$.

For the compressible case, the three velocity equations can be written in wall-normal velocity-vorticity form, which formally reads (see the Appendix)

$$\begin{cases} \mathcal{L}^{c}_{OS}(v) = 0 \\ \mathcal{L}^{c}_{Sq}(\omega_y) = \Delta_h C - \dfrac{dU_b}{dy}\partial_z v \end{cases},$$

where $\mathcal{L}^{c}_{OS}$ and $\mathcal{L}^{c}_{Sq}$ are the corresponding operators in the compressible case to the operators $\mathcal{L}_{OS}$ and $\mathcal{L}_{Sq}$. The term $\Delta_h C$ in the ω_y equation originates from adding a term to the u-equation and another to the w-equation. To remove the coupling term, we set $\Delta_h C = dU_b/dy\,\partial_z v$ and we solve this two-dimensional (2D) Poisson equation at every iteration to determine C. A Fourier spectral method with modified wave number has been used to solve this Poisson equation.

The turbulence decays as a result of removing the coupling term for both $M_\infty=2.5$ and $M_\infty=7.5$. For the lower Mach number, this result is expected from the behavior of the incompressible case. However, the decay at higher Mach number, shown in Fig. 20, constitutes a more interesting result. To our best knowledge, this result is the first direct demonstration that compressible turbulence decays when the non-normality of the underlying linear operator in the nonlinear flow is removed. Therefore, while the formation of the commonly observed near-wall turbulence structures, i.e., streamwise vortices, is known to be essentially nonlinear (e.g., Refs. 27 and 28), the maintenance of the turbulence relies on a linear process. The linear coupling term is necessary to generate the wall-layer streaks, the instability of which in turn is believed to strengthen the streamwise vortices through a nonlinear process. A companion paper addresses this issue and discusses the process of streamwise vortices generation.

IV. CONCLUSION

Predicting the turbulent flow characteristics in a high Mach number boundary layer and studying the associated physical phenomena requires accurate numerical simulations. This represents a twofold challenge for the numerical study: the numerical scheme on one hand and the inflow boundary condition generation algorithm on the other. We have presented a robust and easy-to-implement method for generating the inflow turbulent conditions for compressible turbulent boundary layers. This method allows us to gather turbulence statistics after a short transient time and gives full control of the value of the final R_τ.

To improve our understanding of the fundamental physics of supersonic boundary layers, we have used this method to perform a parametric study varying the free-stream Mach number from 2.5 up to 20 (without taking into account the real gas effects). The turbulence statistics given by the direct numerical simulations are in good agreement with existing results. The van Driest-transformed mean velocity, that is, the density-weighted mean velocity, is found to satisfy the incompressible logarithmic law $u^+_{vd}=1/k\,\log(y^+)+C$, with k and C similar to their incompressible values. When rescaled using the wall quantities, the fluctuations of the velocity and vorticity for different Mach numbers collapse into Guarini's result at $M=2.5$ and therefore into their incompressible counterparts. The budgets of the turbulent kinetic energy are nearly unchanged with increasing Mach number. The maximum of the turbulence production is located around $y^+\approx 10$ and the contribution of the pressure dilatation term remains negligible, consistent with previous observations (e.g., Refs 2 and 4).

We have shown that the apparent increase in the magnitude of the fluctuating Mach number with increasing free-stream Mach number is a variable-property effect. Using the mean density to scale the fluctuating Mach number collapses results for different free-stream Mach numbers. The increase in the pdf tails of the dilatation ϑ, a direct measure of the compressibility, has also been shown to be a variable-property effect. Compressible boundary layers are also shown to be similar to incompressible boundary layers in that, without the linear coupling term, the turbulence cannot be sustained. The linear coupling term is necessary to generate the wall-layer streaks, in spite of the fact that the generation of the streamwise vortices is essentially nonlinear. For an adiabatic wall, the near-wall structure exhibits the same

characteristics as in incompressible turbulent flow in terms of the spanwise spacing of the streaks ($\approx 100^+$) and the spanwise spacing of wall-normal velocity ($\approx 20^+$). Finally, in an isothermal simulation with a cold wall ($\beta_q < 0$), the streaks are longer, whereas for a hot wall ($\beta_q > 0$), they are shorter, in comparison with the simulation with an adiabatic wall ($\beta_q = 0$).

ACKNOWLEDGMENTS

We thank the referees for their constructive comments and suggestions. This work is supported by the NASA Grant/Cooperative Agreement No. NNX08AB39A. The computer time has been provided by NASA Ames Research Center and by NSF TRAC program.

APPENDIX: WALL-NORMAL VELOCITY-VORTICITY FORM

Consider the governing equations for incompressible flow

$$\partial_t u + U_b \partial_x u + v \frac{dU_b}{dy} - \partial_z C = -\partial_x p + r.h.s_u,$$

$$\partial_t v + U_b \partial_x v = -\partial_y p + r.h.s_v,$$

$$\partial_t w + U_b \partial_x w + \partial_x C = -\partial_z p + r.h.s_w,$$

where u, v, and w are the streamwise, wall-normal, and spanwise velocity perturbations and U_b is the base flow. The terms $r.h.s_u$, $r.h.s_v$, and $r.h.s_w$ contain the remaining viscous and nonlinear terms. The terms $-\partial_z C$ and $\partial_x C$ are defined below. By taking the sum of the derivatives of the three equations above, we obtain the pressure equation $\Delta p = -2dU_b/dy\partial_x v$. Then, from the equations of u and w, we get the equation for ω_y. Multiplying the v-equation by v and replacing the pressure term by the equation above, we get the following system for v and ω_y:

$$\begin{cases} \mathcal{L}_{OS}(v) = 0 \\ \mathcal{L}_{Sq}(\omega_y) = \Delta_h C - \dfrac{dU_b}{dy}\partial_z v \end{cases}.$$

Note that Kim and Lim's virtual flow, in which the linear coupling term is not present, is equivalent to setting $\Delta_h C = dU_b/dy\partial_z v$, where $\Delta_h = \partial_{xx} + \partial_{zz}$ is the horizontal Laplacian. Hence, this manipulation corresponds to adding the terms $-\partial_z C$ and $\partial_x C$ in the equations above, where C is computed at every iteration by solving the 2D Poisson equation at every y-location.

For the compressible case, the three velocity equations

$$\partial_t u + U_b \partial_x u + v \frac{dU_b}{dy} - \partial_z C = -\frac{T}{\gamma M_\infty^2}\partial_x p + r.h.s_u,$$

$$\partial_t v + U_b \partial_x v = -\frac{T}{\gamma M_\infty^2}\partial_y p + r.h.s_v,$$

$$\partial_t w + U_b \partial_x w + \partial_x C = -\frac{T}{\gamma M_\infty^2}\partial_z p + r.h.s_w$$

give formally

$$\begin{cases} \mathcal{L}^c_{OS}(v) = 0 \\ \mathcal{L}^c_{Sq}(\omega_y) = \Delta_h C - \dfrac{dU_b}{dy}\partial_z v \end{cases}.$$

To drop the coupling term between the velocity v and the vorticity ω_y, we set $\Delta_h C = dU_b/dy\partial_z v$. A Fourier spectral method with modified wave number is used to solve this Poisson equation.

[1] A. J. Smits and J. P. Dussauge, *Turbulent Shear Layers in Supersonic Flow* (AIP, New York, 1996).
[2] T. Maeder, N. A. Adams, and L. Kleiser, "Direct simulation of turbulent supersonic boundary layers by an extended temporal approach," J. Fluid Mech. **429**, 187 (2001).
[3] S. E. Guarini, R. D. Moser, K. Shariff, and A. Wray, "Direct numerical simulation of a supersonic boundary layer at Mach 2.5," J. Fluid Mech. **414**, 1 (2000).
[4] M. P. Martin, "DNS of hypersonic turbulent boundary layers," AIAA Paper No. 2004-2337, 2004.
[5] S. Pirozzoli, F. Grasso, and T. B. Gatski, "Direct numerical simulation and analysis of a spatially evolving supersonic turbulent boundary layer at M=2.25 ," Phys. Fluids **16**, 530 (2004).
[6] M. Lagha, X. Zhong, J. Eldredge, and J. Kim, "A hybrid WENO scheme for the simulation of shock wave-boundary layer interaction," AIAA Paper No. 2009-1136, 2009.
[7] C.-W. Shu and S. Osher, "Efficient implementation of essentially non-oscillatory shock-capturing schemes," J. Comput. Phys. **83**, 32 (1989).
[8] Y. X. Ren, M. Liu, and H. Zhang, "A characteristic-wise hybrid compact-WENO scheme for solving hyperbolic conservation laws," J. Comput. Phys. **192**, 365 (2003).
[9] T. Lund, X. Wu, and K. Squires, "Generation of turbulent inflow data for spatially developing boundary layer," J. Comput. Phys. **140**, 233 (1998).
[10] G. Urbin and D. Knight, "Large-eddy simulation of a supersonic boundary layer using an unstructured grid," AIAA J. **39**, 1288 (2001).
[11] S. Stolz and N. A. Adams, "Large-eddy simulation of high-Reynolds-number supersonic boundary layers using the approximate deconvolution model and a rescaling and recycling technique," Phys. Fluids **15**, 2398 (2003).
[12] P. Sagaut, E. Garnier, E. Tromeur, L. Larcheveque, and E. Labourasse, "Turbulent inflow conditions for large-eddy simulation of compressible wall-bounded flows," AIAA J. **42**, 469 (2004).
[13] A. Ferrante and S. E. Elghobashi, "A robust method for generating inflow conditions for direct simulations of spatially-developing turbulent boundary layers," J. Comput. Phys. **198**, 372 (2004).
[14] S. Xu and P. M. Martin, "Assessment of inflow boundary conditions for compressible turbulent boundary layers," Phys. Fluids **16**, 2623 (2004).
[15] S. Pirozzoli, M. Bernardini, and F. Grasso, "Characterization of coherent vortical structures in a supersonic turbulent boundary layer," J. Fluid Mech. **613**, 205 (2008).
[16] T. B. Gatski and G. Erlebacher, "Numerical simulation of a spatially evolving supersonic turbulent boundary layer," NASA/TM Report No. 211934, 2002.
[17] G. N. Coleman, J. Kim, and R. D. Moser, "A numerical study of turbulent supersonic isothermal-wall channel flow," J. Fluid Mech. **305**, 159 (1995).
[18] P. G. Huang, G. N. Coleman, and P. Bradshaw, "Compressible turbulent channel flow: DNS results and modeling," J. Fluid Mech. **305**, 185 (1995).
[19] P. Kim (private communication, 2010).
[20] J. Kim, P. Moin, and R. D. Moser, "Turbulence statistics in fully developed channel flow at low Reynolds number," J. Fluid Mech. **177**, 133 (1987).
[21] E. F. Spina, A. J. Smits, and S. K. Robinson, "The physics of supersonic

turbulent boundary layers," Annu. Rev. Fluid Mech. **26**, 287 (1994).
[22]R. Samtaney, D. I. Pullin, and B. Kosovic, "Direct numerical simulation of decaying compressible turbulence and shocklet statistics," Phys. Fluids **13**, 1415 (2001).
[23]S. Pirozzoli and F. Grasso, "Direct numerical simulations of isotropic compressible turbulence: Influence of compressibility on dynamics and structures," Phys. Fluids **16**, 4386 (2004).
[24]L. Duan, I. Beekman, and M. P. Martin, "Direct numerical simulation of hypersonic turbulent boundary layers. Part 2. Effect of wall temperature," J. Fluid Mech. **655**, 419 (2010).
[25]P. Bradshaw, "Compressible turbulent shear layers," Annu. Rev. Fluid Mech. **9**, 33 (1977).
[26]J. Kim and J. Lim, "A linear process in wall-bounded turbulent shear flows," Phys. Fluids **12**, 1885 (2000).
[27]J. M. Hamilton, J. Kim, and F. Waleffe, "Regeneration mechanisms of near-wall turbulence structures," J. Fluid Mech. **287**, 317 (1995).
[28]W. Schoppa and F. Hussain, "Coherent structure generation in near-wall turbulence," J. Fluid Mech. **453**, 57 (2002).